# Laser spectroscopy of metastable palladium at 340 and 363 nm

Ibrahim A. Sulai [1] and Peter Mueller [2]
[1]*Department of Physics and Astronomy, Bucknell University, Lewisburg, Pennsylvania 17837, USA*
[2]*Physics Division, Argonne National Laboratory, Lemont, Illinois 60439, USA*

(Received 3 June 2020; revised 19 August 2020; accepted 14 September 2020; published 9 October 2020)

We report measurements of the isotope shift of the mass 104, 105, 106, 108, and 110 stable palladium isotopes for transitions from the metastable state $4d^9(^2D_{5/2})5s$, $^2[5/2]_3 \rightarrow 4d^9(^2D_{5/2})5p$, $^2[7/2]_4^o$ at 340 nm, and $4d^9(^2D_{5/2})5s$, $^2[5/2]_3 \rightarrow 4d^9(^2D_{5/2})5p$, $^2[3/2]_2^o$ at 363 nm. For $^{105}$Pd, we determine the hyperfine structure of both transitions. The measurements were performed by saturation absorption spectroscopy in a custom-built hollow cathode lamp and will serve as a reference for collinear laser spectroscopy of short-lived neutron-rich palladium isotopes. We also report on the observation of a population inversion for the 363-nm transition under certain discharge conditions.

DOI: 10.1103/PhysRevA.102.042805

## I. INTRODUCTION

High-resolution laser spectroscopy of atomic transitions along an isotopic chain enables the determination of nuclear ground-state properties such as root-mean-square charge radii, magnetic dipole and electric quadrupole moments, and nuclear spin assignments in a model-independent manner [1]. Short-lived, neutron-rich nuclei are especially intriguing as their properties are at the heart of many questions related to the high-density phases of QCD, the origin of the chemical elements in astrophysical processes, and the structure of neutron stars [2]. The region around the magic $Z = 50$ tin isotopes with its two doubly magic isotopes $^{100}$Sn ($N = 50$) and $^{132}$Sn ($N = 82$) has attracted much interest. Recent spectroscopy on a long chain of ($Z = 48$) cadmium isotopes from masses of $A = 110$ to 130 showed a linear progression with $N$—extending over ten odd isotopes—of the nuclear quadrupole moment of the $11/2^-$ isomers of cadmium [3,4]. This trend is reproduced with relativistic density functional theory [5,6] and with the nuclear shell model in which a phenomenological effective charge of the neutron is introduced [4]. Pairing correlation of protons and neutrons is essential to both approaches. Whether the trend persists with two fewer protons is an open question and motivates measurements in ($Z = 46$) palladium, as well as other isotope chains (rhodium, ruthenum) in this region of refractory elements.

Spectroscopy on the short-lived isotopes can only be performed at radioactive ion beam facilities. The high melting temperature of the refractory metals poses a challenge to doing so, as most ion sources rely on the thermal evaporation and subsequent ionization of the produced isotopes. For example, resonant laser ionization has been used to efficiently generate intense beams of palladium after the atoms were vaporized at 2000°C [7]. Alternatively, a helium buffer "gas catcher" allows for the extraction of beams of refractory elements produced online with sufficient efficiency as to perform laser spectroscopy [8] without the additional step of vaporizing the refractory atoms. There are presently plans for experiments on neutron-rich palladium at the Californium Rare Isotope Breeder Upgrade (CARIBU) at the Argonne Tandem Linear Accelertor System (ATLAS) at Argonne National Laboratory, and first measurements of palladium isotopes have been made at the University of Jyväskylä [9]. Both groups perform collinear laser spectroscopy on the refractory beams, as it provides the required spectroscopic resolution and sensitivity to deal with the low isotopic yields available (≈1000 ions/s).

In collinear laser spectroscopy, the ≈10 keV energy atomic (or ionic) beam is overlapped with a laser beam in collinear or anticollinear geometry for resonant excitation of an electronic transition. The acceleration of the atomic beam causes a kinematic compression of the Doppler width and thus a narrowing of the widths of the observed resonances. However, for extracting isotope shifts between isotopes of different masses—and thus different velocities at constant beam energy—the attendant large Doppler shifts require precise calibration of that beam energy or, alternatively, high-precision reference data on stable isotopes. For some of the refractory elements of interest such as the mentioned palladium, rhodium, or ruthenium, such reference data with sufficient precision is lacking for accessible atomic transitions.

In this work, we present the results of saturated absorption spectroscopy (SAS) on stable palladium isotopes. We make use of a see-through hollow cathode lamp, which allows for both optical access and the efficient population of the relevant metastable states. Resonant absorption of laser light is recorded via lock-in detection and combined with a flexible cavity-transfer laser frequency lock to precisely control and calibrate differences in laser excitation frequencies. Applications of this technique can provide reference data for ongoing collinear laser spectroscopy on palladium and other refractory elements.

## II. EXPERIMENTAL DETAILS

There are six stable isotopes of palladium: $^{102}$Pd, $^{104}$Pd, $^{105}$Pd, $^{106}$Pd, $^{108}$Pd, and $^{110}$Pd with 1.02, 11.1, 22.3, 27.3, 26.5, and 11.7 percent natural isotopic abundances,

 

respectively. Mass and nuclear charge distribution differences gives rise to isotope shifts of their atomic energy levels. The nonzero nuclear spin ($I = 5/2$) of $^{105}$Pd gives rise to its hyperfine structure. The even isotopes ($I = 0$) have no hyperfine structure. We measured the two transitions $4d^9(^2D_{5/2})5s,\ ^2[5/2]_3 \rightarrow 4d^9(^2D_{5/2})5p,\ ^2[7/2]^o_4$ at 340 nm and $4d^9(^2D_{5/2})5s,\ ^2[5/2]_3 \rightarrow 4d^9(^2D_{5/2})5p,\ ^2[3/2]^o_2$ at 363 nm. We have obtained independent determinations of the hyperfine constants for the odd isotope and isotope shifts of all stable isotopes (except for $^{102}$Pd) that are on par with or an improvement over the literature values.

For $^{105}$Pd, the hyperfine interaction perturbs the energy of the state $|JIF\rangle$ by

$$\Delta E = \frac{A}{2}C + \frac{B}{4}\frac{\frac{3}{2}C(C+1) - 2(I+1)J(J+1)}{I(2I-1)J(2J-1)} \qquad (1)$$

for $F = J + I$, where $J$ is the total electronic angular momentum, $I$ is the nuclear spin, and $C = F(F+1) - J(J+1) - I(I+1)$. A and B in Eq. (1) represent the magnetic dipole and electric quadrupole constants, respectively. The $E1$ transition matrix elements between two states can be calculated as

$$|\langle JIF||d||J'IF'\rangle|^2 = (2F+1)(2F'+1) \times \begin{Bmatrix} J & F & I \\ F' & J' & 1 \end{Bmatrix} |\langle J||d||J'\rangle|^2, \qquad (2)$$

for the dipole operator $d$. We use Eqs. (1) and (2) along with literature values of the A and B coefficients [10–12] to calculate the positions of the hyperfine levels and the relative intensities of allowed transitions in $^{105}$Pd at 340 and 363 nm. These are shown in Fig. 1.

Both the 340- and 363-nm transitions originate from the metastable $4d^9(^2D_{5/2})5s,\ ^2[5/2]_3$ level. We populate this metastable state by sputtering atoms off a palladium foil in a custom made, see-through hollow cathode lamp (HCL). Subsequent collisions of the atoms in the discharge populate many excited states which cascade down to the metastable state. The see-through design of the lamp enables the transmission of counterpropagating laser beams along the cylindrical axis of the electrodes. We fashion our HCL after the design described by Saini *et al.* [13]. It comprises cylindrical hollow electrodes: a cathode (o.d. = 16 mm, i.d. = 6.5 mm, length = 12 mm), and a pair of anodes (length = 4 mm). The inner surface of the cathode is lined with a foil of enriched $^{105}$Pd for the hyperfine stucture measurements, and with a foil of Pd having natural isotopic composition for the isotope shift determinations.

We mount the electrodes on a standard ConFlat flange, which we then attach to a vacuum system having a pair of optical viewports, ports for pumping, and a leak valve for regulating an equilibrium gas pressure of argon at a few hundred mTorr. We operate the lamp at a DC voltage of 200 to 350 V in a constant current mode ($\approx$ 30 mA) such that the negative glow region is concentrated in the bore of the cathode. Figure 2 shows a schematic of the experiment. The 340- and 363-nm light is produced by frequency doubling the output of an infrared (IR), continuous-wave Ti:sapphire laser. We obtain $\approx$ 20 mW of the second harmonic, which we split into counterpropagating, linearly polarized pump and probe

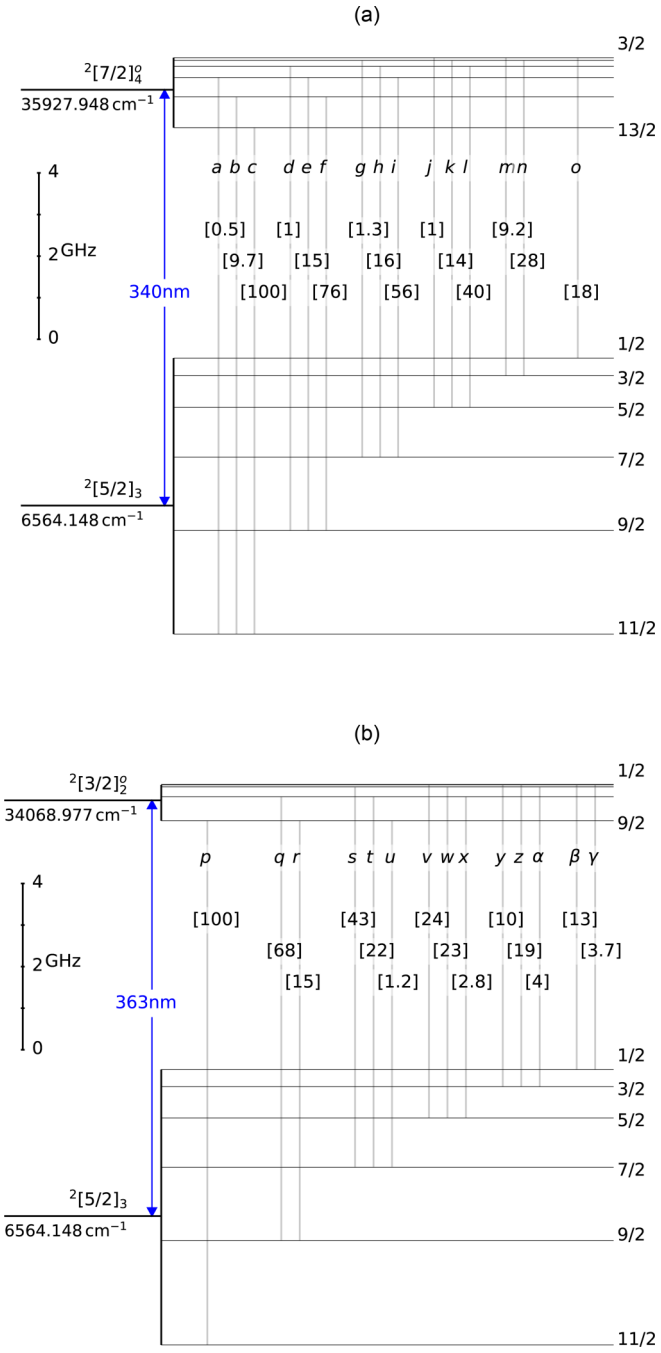


FIG. 1. Level scheme showing the hyperfine splitting in $^{105}$Pd and allowed transitions for the 340-nm line (panel a) and the 363-nm line (panel b). The values in square brackets represent the relative intensities of the allowed transitions, normalized to the strongest lines (transitions c and p). The levels are labeled by their terms and energy values.

beams with intensities of approximately 10$\times$ and 1$\times$ the saturation intensity (71 mW/cm$^2$). We overlap the pump and probe in the volume of the lamp—combining and splitting the beams using polarization beam splitters as shown in Fig. 2. We mechanically chop the pump beam at 2 kHz and demodulate the absorption signal using a lock-in amplifier referenced to the chopper frequency.

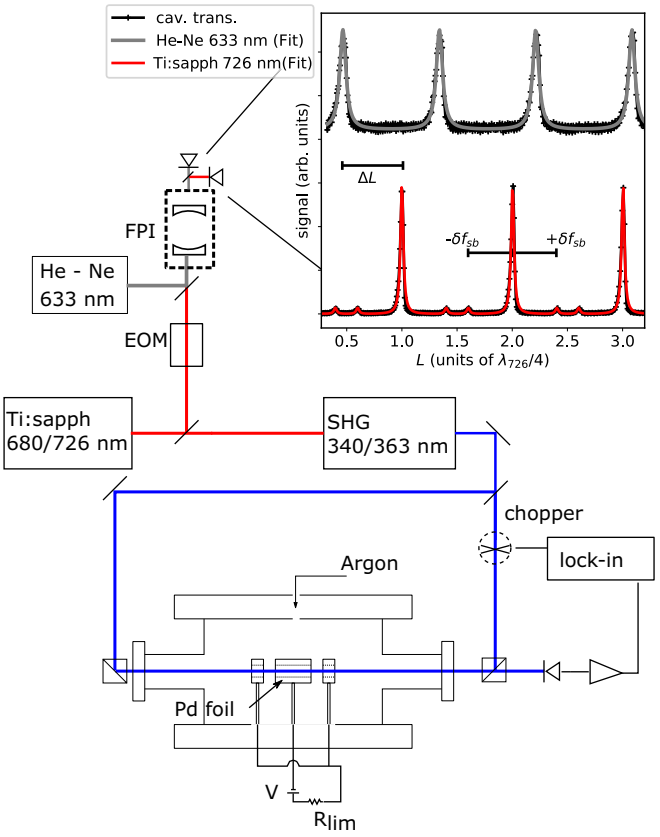


FIG. 2. Schematic of the experimental setup. The 340- and 363-nm light is generated by frequency doubling 680- and 726-nm light from a Ti:sapphire laser, which is referenced to an intensity stabilized He-Ne laser via a scanning Fabry Perot cavity (FPI). RF sidebands at $\pm\delta f_{sb}$ are applied to the 680- and 726-nm light with an EOM to calibrate the FSR of the cavity. In the inset, we show transmission signals for the 633-nm He-Ne and the $\lambda = 726$ nm whose peaks are separated by cavity displacements of $\lambda/4$. The cavity length separation of 726- and 633-nm peaks $\Delta L$ is converted a relative frequency difference via Eq. (3). The hollow cathode lamp (HCL) assembly comprises hollow electrodes, in which we place a palladium foil in an argon buffer gas environment. A discharge is struck by applying a potential across the electrodes, while keeping the current fixed, and limited by $R_{\rm lim}$. The 340- and 363-nm light is used for saturation absorption spectroscopy in the metal vapor established in the HCL. The pump beam is amplitude modulated with a chopper and the absorption signal is demodulated by a lock-in amplifier.

For spectroscopy, we sweep the frequency of the second harmonic at a rate of $\approx 10$ MHz/s across the atomic resonance by scanning the infrared laser and simultaneously recording the probe beam amplitude as well as the lock-in amplifier output. At the same time, we monitor the transmission of the IR light through a scanning, confocal Fabry-Perot interferometer (FPI) of length $d = 150$ mm, whose length is periodically varied with a frequency of 10 Hz by applying a linear voltage ramp $[V(t)]$ to a piezo stack attached to one of the cavity mirrors. In addition and concurrently to the IR light, we pass light from a frequency-stabilized helium-neon laser (Melles Griot 05-STP-901 with 2-MHz long-term frequency stability) through the same cavity to provide a frequency reference $f_0$. Transmission signals of both lasers through the cavity are separately detected on two photodetectors behind a polarizing beam splitter, continuously digitized at 10-kHz rate in sync with the piezo voltage ramp, and saved for further data analysis.

Resonances of the scanned confocal cavity are separated by small cavity length changes $\Delta L = \lambda/4$. For a fixed cavity length and a varying laser frequency, they occur at frequency intervals $\Delta f_{\rm FSR} = c/4d$, the free spectral range of a confocal FPI. When both the laser frequency and cavity length vary, the frequency change of the laser is related to the separation of the cavity resonances via

$$f - f_0 = \frac{\Delta L}{\lambda/4}\Delta f_{\rm FSR} \approx \frac{\Delta f_{\rm FSR}}{\lambda/4}\frac{dL(V)}{dV}\Delta V. \qquad (3)$$

Knowledge of $L(V)$, $\Delta V$, and $\Delta f_{\rm FSR}$ thus allows us to monitor the frequency $f$ of the IR laser using Eq. (3) above.

For a piezo, $L(V)$ is in general a nonlinear function which we obtain in the following manner: First we determine the spacing of adjacent peaks $\Delta V_i = V_{i+1} - V_i$ when the frequency of the laser is kept fixed, where $i$ is the index label of subsequent peaks. As discussed above, the corresponding cavity length change is $\Delta L(V_i) = \lambda/4$, and so we approximate $dL(V_i)/dV \approx \Delta L(V_i)/\Delta V_i = (\lambda/4)/\Delta V_i$. Next, we vary $V_i$ by changing the laser frequency by a few MHz such that we move the cavity resonances to different relative phases of the scan. Finally, we numerically integrate many discrete measurements of $dL(V_i)/dV$ to obtain $L(V)$. Our procedure is similar to the method described in Ref. [14]. The function $L(V)$ enables us to transform the applied voltage into a displacement of the cavity and to compensate for piezo scan nonlinearities. Figure 2 shows typical transmission data and fits for the helium-neon (633-nm) reference and Ti:sapphire (726-nm) transmission peaks to an Airy function. Using Eq. (3), we extract the relative frequency $f$ of the Ti:sapphire laser.

We determine the free spectral range $\Delta f_{\rm FSR}$ of the FPI to be $501 \pm 1$ MHz as follows: We apply sidebands at well-defined frequency $\pm\delta f_{sb}$ with parts-per-million relative uncertainty to the IR laser carrier via a radio-frequency synthesizer and an electro-optical modulator (EOM) and analyze their relative positions in the FPI. The inset in Fig. 2, for example, shows $\pm\delta f_{sb} = 200.00$ MHz sidebands on the cavity transmission of the 726-nm light. The free spectral range is obtained as an average of several such measurements at different sideband frequencies using the linearized piezo displacement function mentioned in the previous paragraph.

## III. RESULTS

The experimental data comprise several wide laser scans that cover all spectral features of each transition, including isotope shift and hyperfine structure of the respective transition. The demodulated amplitude of the saturated absorption signal obtained as a function of the measured laser frequency is shown for a single scan each in Figs. 4 and 5 for the two transitions, respectively; panels (a) and (c) of both figures contain data taken with an isotopically enriched $^{105}$Pd sample, while panels (b) and (d) of both figures show spectra for samples having natural isotopic composition. Because of the limited amount of isotopically enriched Pd available, we only were able to obtain two scans for each transition with

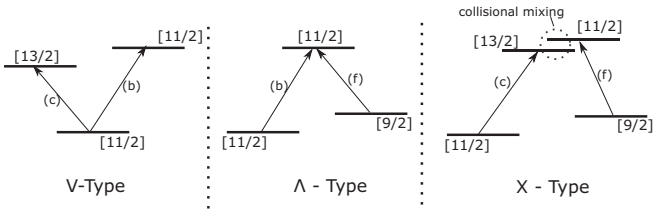


FIG. 3. Examples of level combinations resulting in the crossover resonances: $V_{(b,c)}$, $\Lambda_{(b,f)}$,and $X_{(c,f)}$ lines for the 340 nm transition as indicated in Figure 4(b). The total angular momentum (F) of each level is given in square brackets. For the V-Type and Λ-Type cross overs, the transitions share a common level. For the X-Type, they do not. Crossover lines arise from collisional mixing of the population in the two excited states.

good signal-to-noise ratio. However, these data proved indispensable for unambiguously identifying the many observed transition in this complicated spectrum. With natural Pd foil, up to 15 scans were taken for each. The spectra shown in

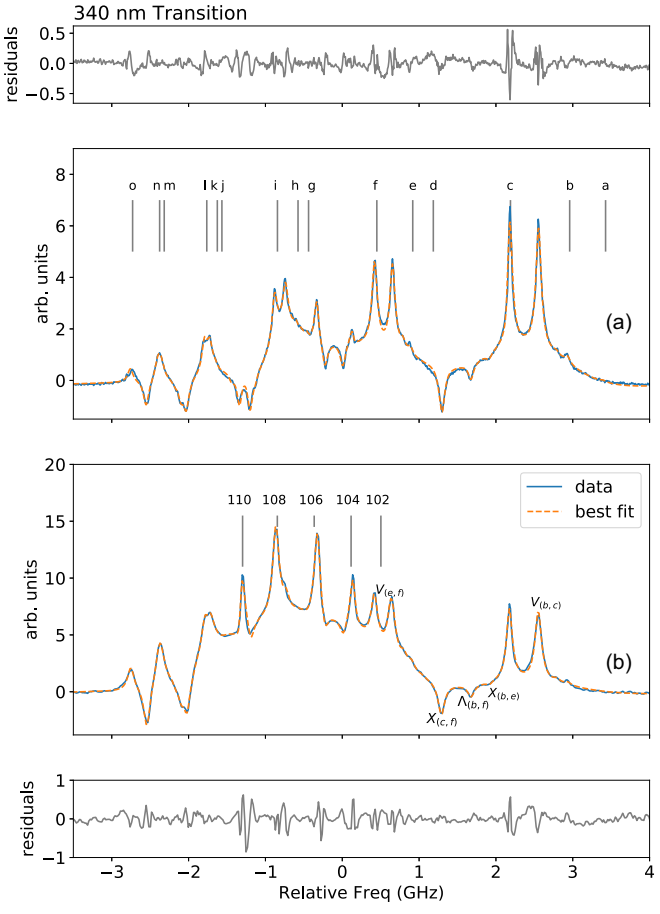


FIG. 4. Spectrum and fit for the 340-nm transition. The fit residuals are shown in the lower and upper panels. Panel (a) shows results from the the $^{105}$Pd isotopically enriched sample. The labeled principal lines a–o correspond to the transitions similarly labeled in Fig. 1. Panel (b) shows a typical spectrum of a sample with natural isotopic abundance from which we measure the positions of the even isotopes. The zero-frequency position corresponds to the $^{105}$Pd center of gravity.

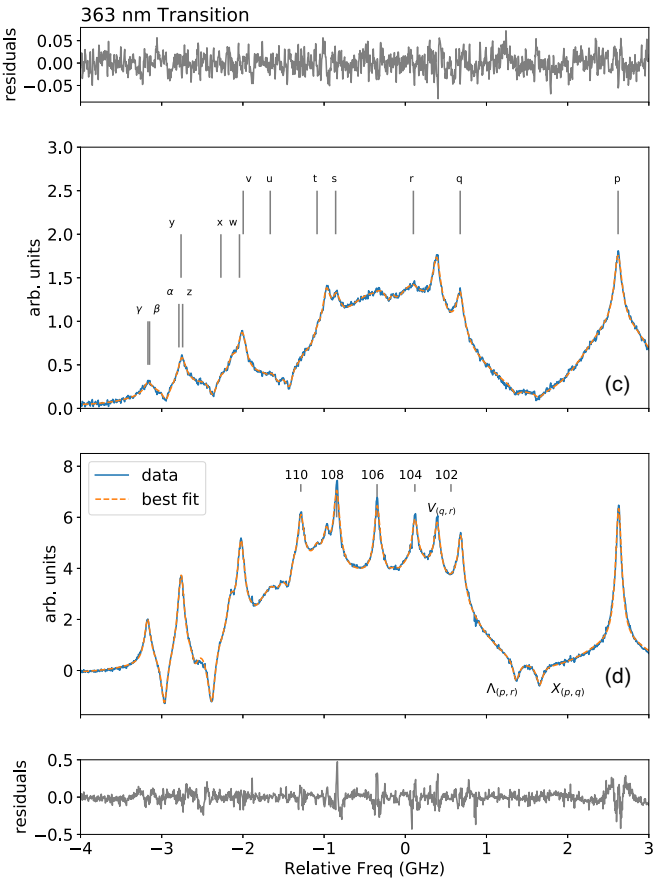


FIG. 5. Spectrum and fit for the 363-nm transition. The fit residuals are shown in the lower and upper panels. Panel (c) shows results from the the $^{105}$Pd isotopically enriched sample. The labeled principal lines p–$\beta$ represent transitions between hyperfine shifted levels as indicated in Fig. 1. Panel (d) shows a typical spectrum of a sample with natural isotopic abundance. The zero-frequency position corresponds to the $^{105}$Pd center of gravity.

Figs. 4 and 5 include data and best fit with a model described in the following paragraphs. At the full-signal scale, data and fit overlap nearly perfectly. Respective fit residuals are plotted in the panels above and below in a magnified scale to enhance observed deviations.

We fit the spectra with the model

$$\text{signal} = \sum_{i=1}^{N} \mathcal{L}_i(f_0, \sigma, a_i, f_i(A_e, B_e, A_g, B_g)) + \sum_{j=1}^{5} \mathcal{L}_j(\sigma, a_j, f_j) + G_{bg}, \quad (4)$$

which is made up of the sum of Lorentzians comprising peaks associated with the odd isotope $\mathcal{L}_i$, peaks associated with the even isotopes $\mathcal{L}_j$, as well as a background $G_{bg}$ composed of the sum of six broad Gaussian functions to account for a residual Doppler broadened background due to detector nonlinearity and residual transfer of the pump beam amplitude modulation onto the Doppler-broadened absorption of the probe beam, presumably via optogalvanic effects on the plasma density and/or collisional population transfer. Only

a single width $\sigma$ is used for all the Lorentzian peaks. The six broad Gaussian peaks were sufficient to account for the background from all the even isotopes and the well-separated strong hyperfine components from $^{105}$Pd toward higher frequency. The $\mathcal{L}_i$ peaks correspond to the principal hyperfine lines, as well as crossover resonances for $^{105}$Pd. Each $\mathcal{L}_i$ is dependent on the following parameters: $^{105}$Pd center of gravity $f_0$, FWHM $\sigma$, amplitude $a_i$, as well as a center frequency $f_i$, which is determined by the hyperfine $A$ and $B$ coefficients of the ground and excited states per Eq. (1). $\mathcal{L}_j$ comprise single peaks of variable amplitude and frequency which represent the even isotopes.

The cross-over resonances occur midway in frequency between pairs of lines which have either a common ground state or a common excited state as illustrated in Fig. 3. In the former case, e.g., between lines b and c in Fig. 1 and corresponding features in Fig. 3(a), the crossover lines have a positive amplitude. We call these $V$-type crossovers. When the lines share a common excited state, e.g., between lines b and f, the crossover resonances have a negative amplitude, and we call them $\Lambda$-type crossovers (middle panel). These are well understood and arise from the velocity class of atoms which have their Doppler shift exactly equal to half the frequency difference between two transitions [15].

In addition to the conventional $\Lambda$- and $V$-type crossover resonances, we also notice crossovers which we denote as X type. Like the $\Lambda$ type, these features have a negative amplitude and occur midway in energy between principal lines, which in this case do not share a common excited state (right panel of Fig. 3). Rather, we deduce that collisional mixing in the plasma must occur rapidly and redistribute population between the two excited states. Such resonances have been observed for example in the work by Ref. [16] and appear to be due to hyperfine changing collisions as discussed in Ref. [17]. Prominent X-type crossovers $X_{cf}$ and $X_{pq}$ are between lines c and f for the 340-nm line and lines p and q for the 363-nm line, respectively, as labeled in Figs. 4(b) and 5(d).

The model described in Eq. (4) accounts for all the principal and crossover resonances, with each line having a FWHM of $\approx$100 MHz. This is about five times the natural linewidth, which is estimated to be 21.3 MHz from lifetime measurements reported in Ref. [18]. This observed width is most likely caused by residual power broadening and is generally consistent with the estimated power density of five to ten times the saturation intensity in the pump beam. Pressure broadening contributes to a lesser amount due to the low Ar operating pressure.

The fit residuals shown in Figs. 4 and 5 indicate deviations of the data from the fit model at the few percent level for the strong peaks—suggesting a mismatch of the assumed Lorentzian line-shape model to the data. As an alternative model, we explored using a sum of pseudo-Voigts instead of a sum of Lorentzian peaks. However, nonzero Gaussian contributions to the peak widths did not improve the fit quality. In addition, we tried a different model in which we allowed the widths of the individual Lorentzian peaks to vary. Our use of a common width for all the Lorentzian peaks in Eq. (4) was based on the well-motivated assumption that all resonances were subject to the same broadening mechanisms. While relaxing this assumption resulted in smaller fit residuals, the isotope shift and hyperfine constants obtained differed by less than 1% from the results obtained from (4). Based on this, we use the model with a common line width for the results that we report. We conclude that at our level of precision, the imperfections of the line-shape model as evident in the residuals do not constitute a dominant source of systematic uncertainty.

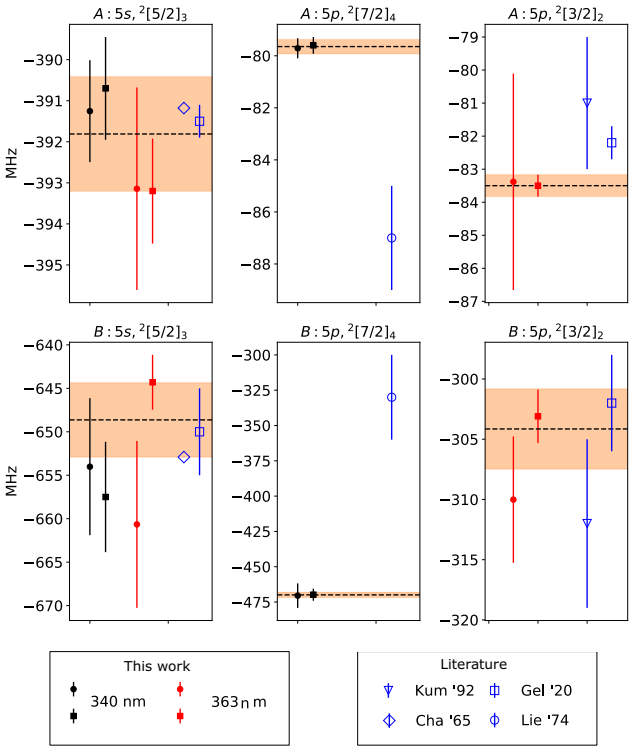


FIG. 6. Hyperfine constant measurements for the $4d^9(^2D_{5/2})5s$, $^2[5/2]_3$, $4d^9(^2D_{5/2})5p$, $^2[7/2]_4$, and $4d^9(^2D_{5/2})5p$, $^2[3/2]_2$ states of Pd-I. The filled circles (squares) are measurements using the $^{105}$Pd-enriched (natural abundance) samples. The band represents the standard error for independent measurements. Results of literature values for the constants obtained from Refs. [9–12] are shown for comparison.

We take the weighted means of independent measurements obtained from each scan as our final results. We combine the statistical and systematic errors (described below) in quadrature to obtain the final uncertainty.

### A. Hyperfine structure

We use spectra from the $^{105}$Pd isotopically enriched sample to unambiguously identify its hyperfine and crossover resonances. We then determine the $^{105}$Pd hyperfine coefficients by fitting the measured spectra with Eq. (4). We use these coefficients as the initial guess for fitting the spectra obtained from natural isotopic abundance samples, allowing the hyperfine constant parameters to vary. In so doing, we obtain independent measurements of the hyperfine constants with each natural isotope spectrum. In Fig. 6, we show the results. Filled circles and filled squares correspond to results from the enriched and natural abundance samples respectively.

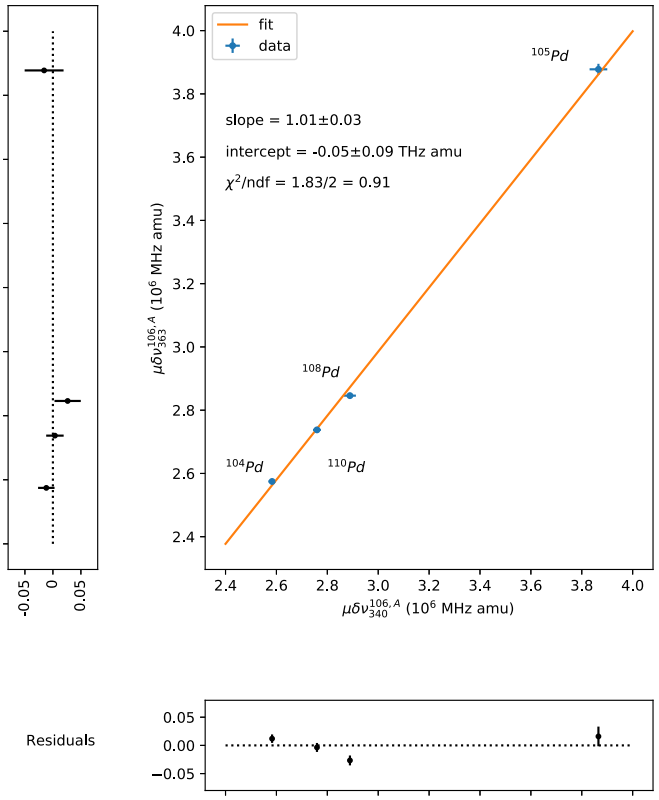


FIG. 7. King plot analysis of the modified isotope shifts for which we use mass 106 as the reference isotope.

Both 340- and 363-nm transitions share the same lower $4d^9(^2D_{5/2})5s$, $J = 3$ level. We obtain consistent values for the hyperfine constants for this level using the two wavelengths (see Fig. 6). Similarly, we use the 340- and 363-nm transitions to determine the hyperfine constants for the $4d^9(^2D_{5/2})5p$, $J = 4$ and $4d^9(^2D_{5/2})5p$, $J = 2$ levels, respectively.

As shown in Fig. 6 and Table I, there is varying degree of agreement with literature. For the lower level, our results are consistent, especially compared to the highly precise measurement of Ref. [10] based on atomic beam magnetic resonance. However, for one of the two upper levels, the $4d^9(^2D_{5/2})5p$, $J = 4$, our measurements disagree with literature values significantly. With regards to the disagreement with Ref. [11], we note that Duijin *et al.* [19] also reported some inconsistency with the former reference for the measurements of hyperfine constants on transitions in the same manifold as the states considered in this work.

TABLE I. Pd-105 hyperfine structure constants.

| Level configuration, term | | This work (MHz) | Lit. (MHz) |
|---|---|---|---|
| $4d^9(^2D_{5/2})5s$, $^2[5/2]_3$ | $A$ | −391.8(1.4) | −391.179(1)[a] |
| | | | −391.5(4)[b] |
| | $B$ | −648.6(4.3) | −652.906(15)[a] |
| | | | −650(5)[b] |
| $4d^9(^2D_{5/2})5p$, $^2[7/2]_4^o$ | $A$ | −79.7(0.3) | −87(2)[b] |
| | $B$ | −469.9(1.8) | −330(30)[b] |
| $4d^9(^2D_{5/2})5p$, $^2[3/2]_2^o$ | $A$ | −83.5(0.3) | −82.2(5)[c] |
| | | | −81(2)[d] |
| | $B$ | −304.1(3.3) | −302(4)[c] |
| | | | −312(7)[d] |

[a]Cha'65 [10].
[b]Lie'74 [11].
[c]Gel'20 [9].
[d]Kum'92 [12]

### B. Isotope shifts

We determined the isotope shifts (IS) of both the 363- and 340-nm transitions from samples having natural isotopic abundance by fitting the measured spectra with Eq. (4) from which we infer the position of all six isotopes. However, the peak from $^{102}$Pd was not clearly resolved above the noise due to its low isotopic abundance of only 1.02%, as well as its overlap with a stronger $^{105}$Pd line. The isotope shifts relative to $^{106}$Pd are reported in Table II. The weighted mean of 12 independent measurements for each transition are used as the isotope shift results. The quoted uncertainty includes both statistical and systematic errors discussed below. We compare our measurements with literature values.

The isotope shift between two isotopes $A$ and $A'$ is $\delta\nu_\lambda^{A,A'} = K_\lambda + F_\lambda\delta\langle r^2\rangle^{A,A'}$, comprising a mass shift contribution $K_\lambda$ and a field shift $F_\lambda\delta\langle r^2\rangle$, where $F_\lambda$ is the electronic structure factor and $\delta\langle r^2\rangle$ is the difference of mean square charge radii. We perform a King plot analysis, shown in Fig. 7 by plotting the modified isotope shifts $\mu\delta\nu_{363}^{106,A}$ and $\mu\delta\nu_{340}^{106,A}$ against each other, using $^{106}$Pd as the reference isotope. The modified isotope shifts for two transitions are hence related via

$$\mu\delta\nu_{363}^{106,A} = f\mu\delta\nu_{340}^{106,A} + k. \tag{5}$$

Here $\mu$ is the inverse mass factor $m_{106}m_A/(m_{106} - m_A)$, and $k = K_{340} - fK_{363}$ relates the field and mass shift, while $f = F_{363}/F_{340}$ is the ratio of the electronic structure factors.

A linear regression to the modified isotope shifts yields $f = 1.01 \pm 0.03$, and an intercept $k = -0.05 \pm 0.09$ THz amu. A deviation of $f$ from unity would indicate a difference of the electronic wave function overlap with the nucleus of the $^2[7/2]_4^o$ and $^2[3/2]_2^o$ states. The intercept enables the determination of the difference of the mass shift contribution to the isotope shifts. As expected, at this level of precision they are

TABLE II. Measured isotope shifts in MHz on the 340- and 363-nm transitions relative to $A = 106$, i.e., $^A$Pd– $^{106}$Pd. Literature results are from Refs. [20] and [9] for which we combine reported statistical and systematic uncertainties in quadrature.

| | 340 nm | | 363 nm | |
|---|---|---|---|---|
| Isotope | This work | Lit. [20] | This work | Lit. [9] |
| $^{102}$Pd | | 938(18) | | 954(20) |
| $^{104}$Pd | 468.6(2.7) | 474(6) | 467.1(1.4) | 461(14) |
| $^{105}$Pd | 347.3(3.1) | | 348.4(1.6) | 344(12) |
| $^{106}$Pd | 0 | 0 | 0 | 0 |
| $^{108}$Pd | −504.7(4.1) | −488(5) | −497.2(1.5) | −492(6) |
| $^{110}$Pd | −946.6(5.4) | −913(13) | −939.2(2.7) | −927(8) |

consistent with 1 and 0, respectively, and any deviations from these values cannot be resolved. Conversely, this agreement and the linearity of the King plot data shows the consistency in isotope shift results between the two transitions.

The errors quoted in Tables I and II are obtained by combining statistical and systematic errors in quadrature. Given $N$ independent measurements of the isotope shift or hyperfine structure (HFS) parameters, we estimate the statistical uncertainty by taking the larger of (1) the error in the weighted least squares fit to a constant or (2) the standard error (i.e., standard deviation / $\sqrt{N-1}$) of the measurements. Fluctuations in the reference laser frequency, and in the FPI cavity peak position determinations contribute to this scatter. However, the variation of the reference laser frequency may also lead to a systematic error. To quantify this, we consider an extreme example whereby the reference frequency drifts linearly by 2 MHz over a the time interval corresponding to a laser scanning across a 10-GHz interval. That would result in a $10^{-4}$ fractional error to the HFS and IS result, and as such is effectively negligible. Another source of systematic uncertainty is the uncertainty in the cavity free spectral range (FSR) $\Delta f_{\mathrm{FSR}}$, which at $501 \pm 1$ MHz results in a fractional uncertainty of $2 \times 10^{-3}$ on the HFS and IS results. This uncertainty in the frequency scale systematically changes all isotope shift and HFS constants by a common factor.

For this work, we operated the HCL with buffer gas (argon) pressure of 0.5 to 1 Torr. This naturally yields some pressure broadening and pressure shifts. We estimate, however, that the pressure shifts do not significantly add systematic errors to the isotope shift and hyperfine constant measurements at the precision of our measurements. The key reason for this is that the pressure shift scales as the polarizability of the states involved in the transition. Therefore, while the total transition energy may have a significant pressure dependence, we expect that to first order (a) the pressure shift is common for all isotopes and (b) the pressure shift is the same for all the levels sharing the same electronic configuration. As a result, pressure shift corrections to the isotope shifts and hyperfine constants are negligible. For example, the fractional shift in the A constant for atomic nitrogen with background argon gas was measured to be on the $10^{-6}$/Torr level [21], significantly smaller than the uncertainty that we report. This assumption is also supported by the fit results at 0.5 Torr shown in Fig. 8 that are consistent with those at 0.2 Torr within our uncertainties, in spite of the manifest signal inversion of the even isotope features.

Finally, we find that the saturation absorption signals have a broad pedestal, with a frequency dependence roughly matching the Doppler-broadened absorption. We attribute this background to the transfer of the pump beam amplitude modulation onto the Doppler-broadened absorption of the probe, as the Pd vapor density depends on the pump beam intensity due to optogalvanic effects on the plasma intensity and collisional dyanmics such as population transfer and velocity-changing collisions [22]. We model this with the background term $G_{bg}$ in Eq. (4), comprising a sum of six Gaussian peaks. This number is motivated by the contributions from the four major even isotopes and the two strongest and most separated hyperfine transitions of $^{105}$Pd. We first fit the Doppler-broadened

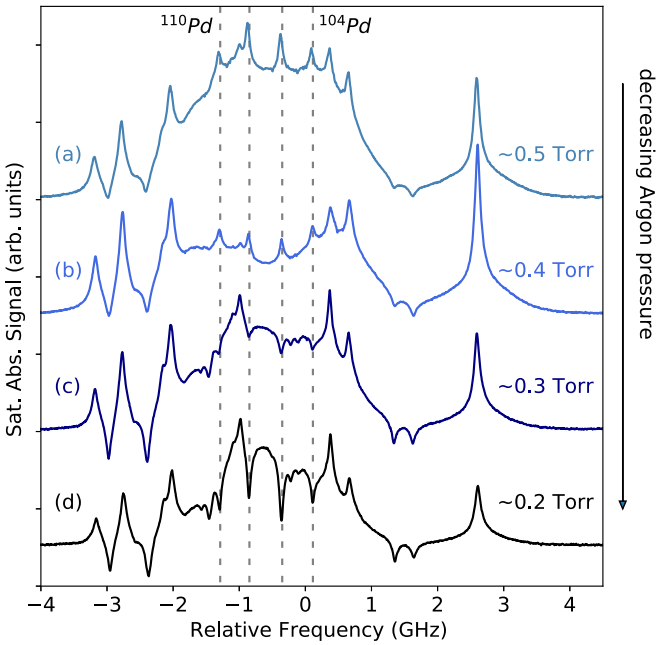


FIG. 8. Inversion of absorption signal from the even isotopes for the 363-nm transition—indicating possible population inversion—as the discharge pressure is varied. The dotted lines from L to R show the positions of $^{110}$Pd, $^{108}$Pd, $^{106}$Pd, and $^{104}$Pd peaks. Features of the $^{105}$Pd isotope did not get inverted.

absorption signal, (i.e. the probe beam amplitude sent to the lock in amplifier) to a set of six Gaussians, and then use the center and width parameters obtained as the initial fit parameters for the components in $G_{bg}$. Subsequently, on fitting the SAS signal, we allow the Gaussian widths to vary by up to 20% of their initial values. We find a slight dependence of the isotope shift and hyperfine constants on the allowed variation range of the $G_{bg}$ peak widths. For example, isotope shift results vary by up to 1 MHz (0.1%), and some of the B coefficients vary by up to 2 MHz (0.7%) when the allowed $G_{bg}$ widths are varied from 5 to 60% of their starting values. We therefore add this variation of the isotope shift and hyperfine constant determinations from each scan to our error budget as a systematic uncertainty due to the background model.

### C. Population inversion at 363 nm

The SAS measurements described above rely on a population buildup in the $4d^9(^2D_{5/2})5s$, $^2[5/2]_3$ metastable state, which is established in the HCL discharge. Subsequent absorption of resonant light drives transitions to the higher lying excited states. While decreasing the buffer gas pressure from $\approx 0.5$ to 0.2 Torr, we observed the inversion of the saturation absorption spectroscopy signal for features of the 363-nm transition associated with the even isotopes. The sign of the resonance flipped from positive to negative, indicating a change from absorption to emission. At pressures lower than 0.2 Torr, the discharge was unstable. We show the spectra obtained while varying the pressure in Fig. 8. Notably, the absorption features from $^{105}$Pd did not change sign in the range of background pressures that we explored. This behavior was only seen on the 363-nm transition and not the 340-nm

transition. We suspect that the observed sign change in the resonance arises from the generation of a population inversion, that is a greater population in the upper $4d^9(^2D_{5/2})5p$, $^2[3/2]_2$ state compared to the $4d^9(^2D_{5/2})5s$, $^2[5/2]_3$ state.

To our knowledge, no one has reported the existence of a population inversion and/or lasing action in palladium. This observation suggests that this 363-nm transition, as well as other transitions connected to the $4d^9(^2D_{5/2})5p$, $^2[3/2]_2$ state, may support laser action in a palladium metal vapor. In future work, we intend on further studying the state-to-state transfer mechanisms for generating this inversion and in exploring lower pressures by constructing lamps with different geometries.

## IV. CONCLUSIONS

We have measured the hyperfine constants of $^{105}$Pd and provide new determinations of palladium isotope shifts on the 340- and 363-nm transitions. These measurements provide new data for characterizing palladium atomic structure and are on par with or are improvements of measurements performed using different techniques. SAS in a custom hollow cathode laboratory is robust and can be used for a range of refractory metals. In addition, it is less sensitive to mass-dependent systematic effects than collinear laser spectroscopy and as such can serve as a reference for planned collinear spectroscopy measurements on neutron-rich isotopes. Finally, we have observed evidence suggesting the existence of a population inversion on the 363-nm transition under low-pressure HCL discharge conditions.

## ACKNOWLEDGMENTS

We are grateful to John P. Greene for providing isotopically enriched Pd samples; to Wilfried Nörtershäuser, the COLLAPS Collaboration, and Kei Minamisono for the loan of critical laser components; and to Felix Sommer and Phillip Ingram for technical support. This work was supported by the US Department of Energy, Office of Science, Office of Nuclear Physics, under Contract No. DE-AC02-06CH11357 and by the US Department of Energy, Office of Science, Office of Workforce Development for Teachers and Scientists (WDTS) under the Visiting Faculty Program (VFP).

[1] E. W. Otten, Nuclear radii and moments of unstable isotopes, in *Treatise on Heavy Ion Science*, edited by D. A. Bromley (Springer, Boston, MA, 1989), Vol. 8, pp. 517–638.
[2] C. J. Horowitz, J. Phys.: Conf. Ser. **312**, 042003 (2011).
[3] N. Frömmgen, D. Balabanski, M. Bissell, J. Bieroń, K. Blaum, B. Cheal, K. Flanagan, S. Fritzsche, C. Geppert, M. Hammen *et al.*, Eur. Phys. J. D **69**, 164 (2015).
[4] D. T. Yordanov, D. L. Balabanski, J. Bieron, M. L. Bissell, K. Blaum, I. Budincevic, S. Fritzsche, N. Frömmgen, G. Georgiev, C. Geppert, M. Hammen, M. Kowalska, K. Kreim, A. Krieger, R. Neugart, W. Nörtershäuser, J. Papuga, and S. Schmidt, Phys. Rev. Lett. **110**, 192501 (2013).
[5] P. W. Zhao, S. Q. Zhang, and J. Meng, Phys. Rev. C **89**, 011301(R) (2014).
[6] D. T. Yordanov, D. L. Balabanski, M. L. Bissell, K. Blaum, I. Budincevic, B. Cheal, K. Flanagan, N. Frömmgen, G. Georgiev, C. Geppert, M. Hammen, M. Kowalska, K. Kreim, A. Krieger, J. Meng, R. Neugart, G. Neyens, W. Nörtershäuser, M. M. Rajabali, J. Papuga, S. Schmidt, and P.W. Zhao, Phys. Rev. Lett. **116**, 032501 (2016).
[7] T. Kron, Y. Liu, S. Richter, F. Schneider, and K. Wendt, J. Phys. B: At., Mol. Opt. Phys. **49**, 185003 (2016).
[8] G. Savard, R. C. Pardo, S. Baker, C. N. Davids, A. Levand, D. Peterson, D. G. Phillips, T. Sun, R. Vondrasek, B. J. Zabransky, and G. P. Zinkann, Hyperfine Interact. **199**, 301 (2011).
[9] S. Geldhof, P. Campbell, B. Cheal, R. de Groote, W. Gins, and I. Moore, Hyperfine Interact. **241**, 41 (2020).
[10] K. H. Channappa and J. M. Pendlebury, Proc. Phys. Soc. **86**, 1145 (1965).
[11] H. Liening, Z. Phys. **266**, 287 (1974).
[12] E. Kümmel, M. Baumann, and C. S. Kischkel, Z. Phys. D - Atoms, Molecules and Clusters **25**, 161 (1993).
[13] V. K. Saini, P. Kumar, K. K. Sarangpani, S. K. Dixit, and S. V. Nakhe, Rev. Sci. Instrum. **88**, 093101 (2017).
[14] W. Bu, M. Liu, D. Xie, and B. Yan, Rev. Sci. Instrum. **87**, 096102 (2016).
[15] W. Demtröder, *Laser Spectroscopy* (Springer-Verlag, Berlin, 2008), Vol. 1.
[16] D. A. Tate and J. P. Walton, Phys. Rev. A **59**, 1170 (1999).
[17] L. Morgus, T. Morgus, T. Drake, and J. Huennekens, Phys. Rev. A **77**, 032704 (2008).
[18] E. Biémont, N. Grevesse, M. Kwiatkowski, and P. Zimmermann, Astron. Astrophys. **108**, 127 (1982).
[19] E. J. van Duijn, S. Witte, R. Zinkstok, and W. Hogervorst, Eur. Phys. J. D **19**, 25 (2002).
[20] P. E. G. Baird, Proc. R. Soc. London A **351**, 267 (1976).
[21] R. H. Lambert and F. M. Pipkin, Phys. Rev. **129**, 1233 (1963).
[22] W. H. Richardson, L. Maleki, and E. Garmire, Phys. Rev. A **36**, 5713 (1987).